arsenic loss before drift of precipitates was started. In one case, oxygen treatment of the arsenic layer induced 40% loss by evaporation from the exposed SiO_2 surface. Therefore, oxidizing atmospheres must be avoided prior to the deposition of protective layers (*e.g.*, polysilicon). In another case, the high dose level lost nearly 70% at the beginning of the temperature gradient anneal due to large inclusions of arsenic extending to the near SiO_2/polysilicon boundary and diffusing into the polysilicon. Additional SiO_2 deposited over the implant, or deeper implants, could be a corrective measure.

Manuscript submitted March 17, 1988; revised manuscript received Aug. 2, 1988.

AT&T Bell Laboratories assisted in meeting the publication costs of this article.

REFERENCES

1. G. K. Celler, L. E. Trimble, K. W. West, L. Pfeiffer, and T. T. Sheng, *Appl. Phys. Lett.*, **50** (11), 664 (1987).
2. G. K. Celler, L. E. Trimble, K. W. West, L. Pfeiffer, and T. T. Sheng, *Mater. Res. Soc. Symp. Proc.*, **92**, 53 (1987).
3. G. K. Celler, L. E. Trimble, T. T. Sheng, K. W. West, S. G. Kosinski, and L. Pfeiffer, *ibid.*, **105**, (1988).
4. H. E. Cline and T. R. Anthony, *J. Appl. Phys.*, **48**, 2196 (1977).
5. G. K. Celler, *CRC Crit. Rev. Solid State Mater. Sci.*, **12**, 193 (1985).
6. G. K. Celler, L. E. Trimble, and L. O. Wilson, *Mater. Res. Soc. Symp. Proc.*, **35**, 635 (1985).
7. Y. Wada and D. A. Antoniadis, *This Journal*, **128**, 1317 (1981).
8. R. Singh, M. Maier, H. Krautle, D. R. Young, and P. Balk, *ibid.*, **131**, 2645 (1984).
9. A. H. van Ommen, *J. Appl. Phys.*, **56**, 2708 (1984).
10. T. R. Anthony and H. E. Cline, *ibid.*, **43**, 2473 (1972).
11. P. G. Shewmon, *Trans. Metal. Soc. AIME*, **230**, 1134 (1964).
12. H. J. Lewerenz and H. Wetzel, *This Journal*, **130**, 1228 (1983).
13. M. Hansen, "Constitution of Binary Alloys," p. 180, McGraw Hill, Inc., New York (1958).

Uniformity of Etching in Parallel Plate Plasma Reactors

Demetre J. Economou,* Sang-Kyu Park, and Gary D. Williams**

Department of Chemical Engineering, University of Houston, Houston, Texas 77204-4792

ABSTRACT

A two-dimensional transport and reaction model of a high pressure (~1 torr) high frequency (13.56 MHz) single-wafer parallel plate plasma reactor was developed. The chemical etching uniformity was studied as a function of reactor operating conditions. The ratio of the reactivity of the surrounding electrode surface as compared to that of the wafer surface, S, critically affected uniformity. A bullseye clearing pattern was predicted for $S < 1$, and the reverse pattern for $S > 1$, while etching was uniform for $S = 1$. In the case of $S \neq 1$, and for the parameter range studied, the absolute uniformity was found to improve by surrounding the wafer with a material of similar reactivity, by increasing the flow rate, or by decreasing the reactor pressure or power. However, such actions also served to decrease the etch rate. The oxygen plasma was used as a model experimental system to test the theoretical predictions. An experimental technique based on spatially resolved optical emission spectroscopy in concert with actinometry and the Abel transform was developed to obtain a three-dimensional mapping of the reactant (O atom) concentration profile in the plasma reactor. When a reactive film was covering part of the substrate electrode, a profound decrease in the reactant concentration was observed over the film. At the same time, large concentration gradients developed, especially at the boundary of the reactive film with the surrounding electrode. Good quantitative agreement was found between the model predictions and the experimental reactant concentration data for the range of pressure, power, flow rate, and reactive film radius examined.

Chemically reactive plasmas are widely used in the microelectronics industry for etching and deposition of thin films (1). The process involves generating a low pressure gas discharge (usually at RF or microwave frequencies) in which relatively inert gases are dissociated to form reactive atoms and radicals. The reactants are transported by convection and diffusion to the substrate surface where they react to form volatile products, thereby etching the substrate, or react to deposit a thin film. The surface reactions are greatly influenced by energetic particle (especially positive ion) bombardment. Owing to the nonequilibrium nature of the plasma and the plethora of reactions involved (for most of which the kinetics is unknown), it is very difficult to predict the flux and energy of particles striking the substrate, and in turn to predict the reaction rate.

Recently there has been much interest in developing models of the plasma etching process. In developing such models there are a number of important phenomena which need be considered. Such phenomena include glow discharge chemistry, electron density and energy distribution, ion transport in the sheath, heat and mass transfer, and heterogeneous reaction kinetics. Even if the kinetics were known, the computational power of present state-of-the-art computers does not allow one to include details of all the above phenomena in a model. Therefore one focuses on specific aspects of the overall process. Published plasma reactor models emphasize the discharge chemistry (2, 3), the discharge physics (4-6), or transport and reaction phenomena (7, 8) including relatively detailed chemical kinetics (9, 10). The above cited and other works have provided much insight into the intricate nature of plasma processes. Nevertheless, the search for a global model with predictive capabilities over a wide range of operating parameters continues.

Owing to the complexity of the plasma etching process, mathematical models must be tested with experimental data taken under well-controlled conditions. *In situ* plasma diagnostics including optical techniques such as optical emission spectroscopy (OES) and laser induced fluorescence (LIF) (11), mass spectrometry and ion energy analysis (12), and Langmuir probe measurements (13) have been employed successfully to gain basic understanding of reactive plasmas. Optical diagnostics are particularly attractive because of their nonintrusive nature. Although LIF is generally more powerful than OES, the latter is much cheaper and easier to implement. Spatially resolved optical emission spectroscopy can provide valuable information on the concentration distribution of active species in a plasma reactor.

The ultimate goal of plasma etching is to obtain a high and uniform etch rate with good anisotropy and selectivity and without radiation damage. Etching nonuniformity is encountered in both volume-loading etchers (14) and in parallel plate etchers, and is of major concern (15). Uniformity problems may become worse as wafer size in-

*Electrochemical Society Active Member.
**Electrochemical Society Student Member.

creases and as new gas formulations yielding faster etch rates are developed. Nonuniform etching necessitates over-etching which can result in substrate damage and/or rapid mask undercut owing to loading. Both phenomena adversely affect device yields. In the case of deep trenches, etching must be uniform for the trench capacitors to have a tight capacitance distribution (18). Etch nonuniformity may be the result of gradients in etchant concentration, in ion bombardment flux and/or energy, or in wafer surface temperature. Nagy (16) and Selwyn (17) found etchant concentration gradients at the boundary where two surfaces with different reactivity met. Such concentration gradients are thought to be responsible for the often-observed "bullseye" clearing pattern, in which the etch rate decreases monotonically from the wafer periphery to its center (19). Although several studies on uniformity of etching have appeared in the literature, no systematic study coupling both theory and experiment has been presented.

Recently, a transport and reaction model of a single-wafer parallel plate plasma reactor was formulated (20). The oxygen plasma etching polymer was chosen as a model experimental system. Good qualitative agreement was obtained between the model predictions and measured etch rates as a function of pressure, power, and flow rate.

In the present work, an extension of the previous model is presented. Given the surface reaction kinetics, the two-dimensional model is capable of predicting both etch uniformity and anisotropy. The present paper emphasizes the uniformity aspect. An experimental technique based on spatially resolved optical emission spectroscopy was developed to obtain a three-dimensional mapping of the etchant concentration profiles. Although spatially resolved OES has been used extensively to map the plasma emission along planes parallel to the discharge electrodes (21), studies of emission profiles along the wafer radius are scarce. Such profiles were obtained in an oxygen discharge in both an empty reactor (no reactive film) and a loaded reactor (with a reactive film covering part of the substrate electrode). The radial emission profiles were then converted to etchant species concentration profiles. The experimental results were compared with the mathematical model predictions. The effect of power, pressure, flow rate, and reactive film radius on the etch uniformity was studied.

Model Formulation

The model was developed for a radially symmetric single-wafer parallel plate plasma reactor shown schematically in Fig. 1. Feed gas enters uniformly through the upper porous wall electrode. Etching products and unreacted feed gas are pumped radially outwards. The wafer was assumed to be in good thermal and electrical contact with the substrate grounded electrode. Hence the wafer surface temperature was assumed constant. Gas temperature variations were also neglected. The primary focus of this work was on the concentration distribution of the etchant species and its effect on etching uniformity. In particular, due to etchant consumption on the wafer surface, large radial concentration gradients may develop, especially at the boundary between the wafer and the surrounding electrode. Since the etching rate is usually a function of the local etchant concentration, the result is etching nonuniformity. Transport and reaction principles were used to analyze the reactant concentration distribution.

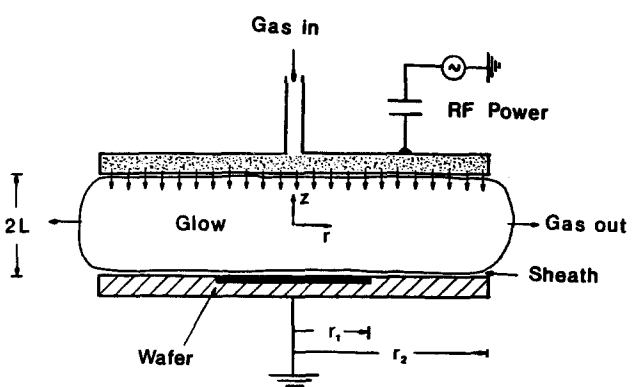

Fig. 1. Schematic of the single-wafer parallel plate etching reactor studied.

Gas flow distribution.—Gas flow resembles the three-dimensional, axisymmetric stagnation point flow (22). Assuming constant gas physical properties and negligible volume change during reaction, the momentum equations can be decoupled from the mass and heat transfer equations. Invoking the continuum approximation which is valid for pressure above about 0.25 torr (for typical reactor dimensions), the Navier-Stokes equations and the continuity equation read (see List of Symbols for meaning of symbols)

$$U\frac{\partial U}{\partial r}+\frac{W}{L}\frac{\partial U}{\partial \zeta}=-\frac{1}{\rho}\frac{\partial P}{\partial r}+\nu\left(\frac{\partial^2 U}{\partial r^2}+\frac{1}{r}\frac{\partial U}{\partial r}-\frac{U}{r^2}+\frac{1}{L^2}\frac{\partial^2 U}{\partial \zeta^2}\right) \quad [1]$$

$$U\frac{\partial W}{\partial r}+\frac{W}{L}\frac{\partial W}{\partial \zeta}=-\frac{1}{\rho L}\frac{\partial P}{\partial \zeta}+\nu\left(\frac{\partial^2 W}{\partial r^2}+\frac{1}{r}\frac{\partial W}{\partial r}+\frac{1}{L^2}\frac{\partial^2 W}{\partial \zeta^2}\right) \quad [2]$$

$$\frac{\partial U}{\partial r}+\frac{U}{r}+\frac{1}{L}\frac{\partial W}{\partial \zeta}=0 \quad [3]$$

where $\zeta = z/L$ is a dimensionless axial coordinate. The boundary conditions are

$$U = 0 \quad \text{at} \quad z = \pm L \text{ for all } r \quad [4]$$

$$W = 0 \quad \text{at} \quad z = -L \text{ for all } r \quad [5]$$

$$W = -W_w \quad \text{at} \quad z = L \text{ for all } r \quad [6]$$

where W_w is the uniform gas velocity at the entrance to the reactor. By setting

$$U = rf'(\zeta)\left(\frac{W_w}{2L}\right) \quad [7]$$

$$W = -W_w f(\zeta) \quad [8]$$

the continuity equation is automatically satisfied. Here $f(\zeta)$ is a function of ζ only and $f'(\zeta) = df/d\zeta$. Inserting Eq. [7] and [8] into Eq. [1] and [2] and eliminating the pressure P, results

$$f'''' + 2R_w ff''' = 0 \quad [9]$$

Hence the flow Eq. [1]-[3] have been reduced to a fourth-order ordinary differential equation. The pertinent boundary conditions are

$$f'(\pm 1) = f(-1) = 0 \quad [10]$$

$$f(1) = 1 \quad [11]$$

The wall Reynolds number is defined as $R_w = W_w L/2\nu$. After solving Eq. [9] subject to boundary conditions Eq. [10] and [11] to obtain $f(\zeta)$ and $f'(\zeta)$, the radial and axial velocity components can be obtained by using Eq. [7] and [8], respectively. In general, Eq. [9] must be solved by numerical techniques. An approximate analytic solution can be obtained, however, for values of the wall Reynolds number sufficiently less than unity. Such a solution may be useful since for typical parameter values $R_w < 1$. By using regular perturbation techniques (23), the following approximate solution was obtained

$$U = \frac{W_w}{2L} r\left[\left(-\frac{3}{4}\zeta^2+\frac{3}{4}\right)+R_w\left(-\frac{1}{160}\zeta^6+\frac{3}{32}\zeta^4+\frac{1}{4}\zeta^3-\frac{117}{1120}\zeta^2-\frac{1}{4}\zeta+\frac{19}{1120}\right)\right] \quad [12]$$

$$W = -W_w\left[\left(-\frac{1}{4}\zeta^3 + \frac{3}{4}\zeta + \frac{1}{2}\right) + R_w\left(-\frac{1}{1120}\zeta^7 + \frac{3}{160}\zeta^5 + \frac{1}{16}\zeta^4 - \frac{39}{1120}\zeta^3 - \frac{1}{8}\zeta^2 + \frac{19}{1120}\zeta + \frac{1}{16}\right)\right] \quad [13]$$

For values of $R_w << 1$, Eq. [12] reduces to

$$U = \frac{3}{8}\frac{W_w}{L}r\left[1 - \left(\frac{z}{L}\right)^2\right] \quad [14]$$

Hence, under the condition $R_w << 1$, the radial velocity profile is parabolic and symmetric with respect to the plane $z = 0$. Since a wide range of flow rates (values of R_w) were examined in the present investigation, numerical solution of Eq. [9] was performed to obtain the gas velocity profiles. These profiles were then used in the convective-diffusion equation to describe etchant transport and reaction.

Etchant transport and reaction.—The model was applied to a diatomic gas A_2 which upon dissociation in the plasma produces atomic etchant species A. Examples include the O_2 and Cl_2 plasmas. Emphasis was placed on the operating regime of typical single-wafer reactors (~1 torr, 13.56 MHz). Under such conditions, the glow is usually sustained by bulk ionization. Therefore, secondary electron emission was neglected. In addition, above the ion transit frequency [~3 MHz, Ref. (12)], ions respond to an average sheath voltage. Therefore, a time-averaged model of the sheath may be used to obtain the ion bombardment flux and energy (24). Some modulation may occur in the electron energy distribution at 13.56 MHz (25), which in turn will modulate the etchant production rate by electron impact dissociation. However, the etchant losses occur on a time scale much longer than that of etchant production. Hence a time-independent etchant concentration should be established. The steady-state etchant species mass balance then reads

$$U\frac{\partial C_1}{\partial r} + W\frac{\partial C_1}{\partial z} = D_1\left[\frac{1}{r}\frac{\partial}{\partial r}\left(r\frac{\partial C_1}{\partial r}\right) + \frac{\partial^2 C_1}{\partial z^2}\right] + 2k_p n_e C_2 - R_v \quad [15]$$

The second term on the right-hand side of Eq. [15] represents etchant production by electron impact dissociation of parent molecules

$$A_2 + e \xrightarrow{k_p} 2A + e \quad [R1]$$

The production rate constant, k_p, depends on the electron energy distribution function and the cross section for the reaction. For a Maxwellian electron distribution function

$$k_p = \sqrt{\frac{8}{\pi m}}(kT_e)^{-\frac{3}{2}}\int_0^\infty \epsilon_e \sigma(\epsilon_e)\exp\left(-\frac{\epsilon_e}{kT_e}\right)d\epsilon_e \quad [16]$$

The electron energy varies with position, especially along the axial direction. Electrons pick up energy from the oscillating sheaths resulting in higher electron energy at the sheath/glow boundaries. A spatially-averaged value of k_p was used in this work. This is not expected to significantly affect the radial etchant concentration profiles, especially for a small interelectrode gap.

Two forms of the electron density profile were examined. Uniform electron density ($n_e = \bar{n}_e$), and the profile corresponding to a diffusion-controlled discharge in a cylindrical container (26)

$$n_e(r, z) = n_{eo}J_0\left(2.405\frac{r}{r_2}\right)\cos\left(\frac{\pi z}{2L}\right) \quad [17]$$

where J_0 is the zeroth order Bessel function of the first kind.

The third term on the right-hand side of Eq. [15] represents etchant elimination by volume reactions. A typical example is etchant recombination according to

$$A + A + M \xrightarrow{K_v} A_2 + M \quad [R2]$$

where M is a third body needed to conserve both energy and momentum during recombination. Volume recombination is especially important at higher pressures. The pertinent reaction rate can be expressed as $R_v = K_v C_1^2 C_M$. Surface reactions enter in the boundary conditions described below

$$\frac{\partial C_1}{\partial r} = 0 \quad \text{at } r = 0, \quad -L \le z \le L \quad [18]$$

$$\frac{\partial C_1}{\partial r} = 0 \quad \text{at } r = r_2, \quad -L \le z \le L \quad [19]$$

$$-D_1\frac{\partial C_1}{\partial z} - W_w C_1 = k_c C_1 \quad \text{at } z = L, \ 0 \le r \le r_2 \quad [20]$$

$$D_1\frac{\partial C_1}{\partial z} = k_a C_1 \quad \text{at } z = -L, \quad r_1 < r \le r_2 \quad [21]$$

$$D_1\frac{\partial C_1}{\partial z} = R_t \quad \text{at } z = -L, \quad 0 \le r \le r_1 \quad [22]$$

Equation [18] is a symmetry condition and Eq. [19] is a simplified exit boundary condition. Equation [20] accounts for both etchant convection away from and etchant recombination on the upper electrode surface. A first-order recombination reaction has been assumed (27). Equation [21] describes surface recombination on the part of the lower electrode surrounding the wafer. The surface recombination rate may be written as the product of the etchant flux striking the surface ($1/4\ v_1 C_1$) and the wall recombination coefficient w. The corresponding reaction rate constant is then $k_i = 1/4\ v_1 w_i$ with $i = a, c$. Equation [22] describes etching on the wafer surface. Recombination was neglected compared to etching on the wafer surface. The surface reaction kinetics is complex and very little understood, especially the effect of ion bombardment. Ions may create "active" sites on the surface where reaction of neutrals can proceed faster and/or ions may "clear" the surface by sputtering adsorbed species or polymeric films and exposing "fresh" surface sites for further reaction to occur (28, 29). For modeling purposes, the following simplified kinetic model was used based on the surface "damage" mechanism (30)

$$A_2^+ + S \xrightarrow{k_d} S^* \quad [R3]$$

$$A + S \xrightarrow{k_n} P \quad [R4]$$

$$A + S^* \xrightarrow{k_+} P \quad [R5]$$

In Eq. [R3] positive ions (mainly molecular ions A_2^+) bombard the surface and create "damaged" surface sites S^*. Etchant A can react on both undamaged and damaged surface sites (Eq. [R4] and [R5], respectively), perhaps faster on the latter, to produce P. Sputtering of the surface by ion bombardment has been neglected, but it can be easily accounted for. The total etch rate is

$$R_t = (k_+ C_1)\left(\frac{k_d \epsilon_+ I_+ + k_n C_1}{k_d \epsilon_+ I_+ + k_+ C_1}\right) \quad [23]$$

where the reaction rate of [R3] has been assumed proportional to the ion flux I_+ and the average ion energy ϵ_+. Reactions [R4] and [R5] have been assumed first-order in etchant concentration C_1. The degree of anisotropy is defined

as the ratio of the ion-assisted reaction rate [R5] to the total reaction rate R_t. Then

$$An = \frac{k_d I_+ \epsilon_+}{k_d I_+ \epsilon_+ + k_n C_1} \quad [24]$$

For large ion flux and/or energy or for slow chemical etching reaction (small k_n), the degree of anisotropy approaches unity, *i.e.*, highly anisotropic etching results. One observes from Eq. [23] that for large ion to etchant fluxes (large I_+/C_1), the rate is simply k_+C_1, *i.e.*, the rate is limited by the etchant supply. In the absence of ion bombardment ($I_+ = 0$), Eq. [23] reduces to $R_t = k_nC_1$, *i.e.*, only chemical (isotropic) etching occurs.

At sufficiently high gas flow rates, the etching reaction product concentration in the plasma will be low. Assuming that A is the only important etchant, and that the major components in the plasma are A and A_2, Eq. [15] suffices to determine the etchant concentration distribution. The parent molecule concentration can then be found as

$$C_2 = C_t - C_1 = \frac{P}{R_g T_g} - C_1 \quad [25]$$

The etchant mass balance Eq. [15] was nondimensionalized by using

$$\theta_1 = \frac{C_1}{C_t} \quad \theta_e = \frac{n_e}{\bar{n}_e} \quad \zeta = \frac{z}{L} \quad \text{and } \xi = \frac{r}{r_2} \quad [26]$$

The dimensionless equation is

$$\mathrm{Pe}\, A \left[\xi f'(\zeta) \frac{\partial \theta_1}{\partial \xi} - 2 f(\zeta) \frac{\partial \theta_1}{\partial \zeta} \right] = \left[\frac{1}{\xi} \frac{\partial}{\partial \xi} \left(\xi \frac{\partial \theta_1}{\partial \xi} \right) + A^2 \frac{\partial^2 \theta_1}{\partial \zeta^2} \right] + \mathrm{Da}\,(1 - \theta_1)\theta_e - \beta_1 \theta_1^2 (1 - \theta_1) \quad [27]$$

The dimensionless boundary conditions are

$$\frac{\partial \theta_1}{\partial \xi} = 0 \quad \text{at } \xi = 0, 1 \quad -1 \le \zeta \le 1 \quad [28]$$

$$-A \frac{\partial \theta_1}{\partial \zeta} = (\gamma_c + 2\mathrm{Pe})\theta_1 \quad \text{at } \zeta = +1 \quad 0 \le \xi \le 1 \quad [29]$$

$$A \frac{\partial \theta_1}{\partial \zeta} = \gamma_a \theta_1 \quad \text{at } \zeta = -1 \quad \xi_1 < \xi \le 1 \quad [30]$$

$$A \frac{\partial \theta_1}{\partial \zeta} = \Phi_+ \theta_1 \left(\frac{\delta \epsilon_+^* I_+^* + \theta_1}{\delta \epsilon_+^* I_+^* + \theta_1 \Phi_+ / \Phi_n} \right) \quad \text{at } \zeta = -1 \quad 0 \le \xi \le \xi_1 \quad [31]$$

In Eq. [27]

$$\theta_e = \begin{cases} 1 \text{ or} & [32a] \\ 3.64\, J_0(2.405\,\xi) \cos(\pi/2\,\zeta) & [32b] \end{cases}$$

depending on the electron density profile used. Other dimensionless quantities in Eq. [27] are

$$A = \frac{r_2}{L} \quad \mathrm{Pe} = \frac{W_w r_2}{2D_1} = \frac{Q}{2\pi D_1 r_2} \quad [33]$$

$$\mathrm{Da} = \frac{2k_p \bar{n}_e r_2^2}{D_1} \quad \beta_1 = \frac{K_v C_t^2 r_2^2}{D_1} \quad [34]$$

Functions $f(\zeta)$ and $f'(\zeta)$ were found by solving Eq. (9). Further, in Eq. [29]-[31]

$$\Phi_n = \frac{k_n r_2}{D_1} \quad \Phi_+ = \frac{k_+ r_2}{D_1}$$

$$\gamma_c = \frac{k_c r_2}{D_1} = \frac{v_1 w_c r_2}{4D_1} \quad \gamma_a = \frac{k_a r_2}{D_1} = \frac{v_1 w_a r_2}{4D_1} \quad [35]$$

$$\delta = \frac{k_d \bar{n}_e k T_e u_R}{k_n C_t} \quad \epsilon_+^* = \frac{\epsilon_+}{kT_e}$$

$$u_R = (kT_e/M_2)^{1/2} \quad I_+^* = \frac{I_+}{n_e u_R} \quad [36]$$

The Peclet number, Pe, shows the relative importance of convection as compared to diffusion. The Damköhler number, Da, shows the relative significance of etchant production as compared to diffusion. For large values of Da, the etchant is produced faster than it can diffuse, resulting in nonuniform concentration profiles. Dimensionless grouping β_1 is analogous to Da, except that it involves the volume recombination reaction rate instead of the production rate. In Eq. [35], the Thiele modulus Φ_n describes the effects of chemical etching as compared to diffusion. If etching is fast (large k_n) or the diffusivity is low (*e.g.*, high pressure), large reactant concentration gradients may develop, depending on the reactivity of the wafer compared to that of the surrounding electrode. Groupings Φ_+, γ_a, and γ_c are analogous to Φ_n except that the chemical etching reaction rate constant is replaced by the ion-assisted etching reaction rate constant (Φ_+) or by the wall recombination rate constant (γ_a and γ_c). Grouping δ gives a measure of the degree of anisotropy attained. When δ is large, the ion-assisted reaction dominates and anisotropic etching is expected (also see Eq. [38]).

Quantities ϵ_+^* and I_+^* are the dimensionless ion bombardment energy and flux, respectively. Such quantities may be obtained from a sheath model described elsewhere (24). [The ion energy ϵ_+^* as defined here differs from Ref. (24) by a factor of 2]. Important parameters of such models are the dimensionless sheath voltage (V_S^*) and the ion collision number (Co). The latter is a measure of the number of collisions an ion suffers in its transit through the sheath

$$V_S^* = V_S/kT_e \quad Co = N\lambda_D \sigma_t/2 \quad [37]$$

Finally, taking into account Eq. [36], the degree of anisotropy (Eq. [24]) may be rewritten as

$$An = \frac{\delta I_+^* \epsilon_+^*}{\delta I_+^* \epsilon_+^* + \theta_1} \quad [38]$$

The method of solution consisted of solving Eq. [9] by a finite difference method to obtain $f(\zeta)$ and $f'(\zeta)$ and subsequently solving Eq. [27] by a finite element method. Two approaches were taken. First, values of the pertinent dimensionless groups were prescribed and their effect on etch rate, uniformity, and anisotropy was studied. Second, the oxygen plasma was chosen as a model system and parameter values specific to this system were used for the operating conditions of our experimental plasma etching reactor to be described in the next section. The purpose was to test the model predictions in terms of etchant concentration and its profile as a function of pressure, power, flow rate and reactive film radius.

Experimental

A schematic of the experimental setup is shown in Fig. 2. The parallel plate single-wafer etcher had a 13.1 cm diam, hard anodized aluminum powered showerhead upper electrode held at a distance of 2.2 cm from the 13.9 cm diam aluminum grounded lower electrode. The temperature of both electrodes was controlled with a closed-loop system (Bay Voltex, Tempryte, HS-3500-WC-DC-SX) and the lower electrode temperature was monitored with an embedded Fe-constantan thermocouple. Gases were pumped by a two-stage rotary vane pump (Edwards, E2M40) and the base pressure was less than 1 mtorr. Chamber pressure and gas flow rate were independently controlled by a closed-loop system composed of a pressure

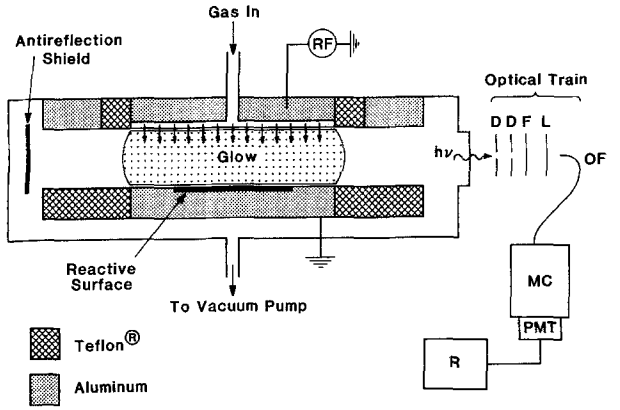

Fig. 2. Schematic (not drawn to scale) of the experimental plasma reactor and optical emission spectroscopy system. D: iris diaphragm, F: optical filter, L: lens, OF: optical fiber, MC: monochromator, PMT: photomultiplier tube, R: recorder.

transducer (MKS 222B), an exhaust throttle valve (MKS 253) and a controller (MKS 252A). Gas flow rate was regulated by mass flow controllers (MKS 1259A). The gases used were extra dry oxygen and prepurified argon (used as actinometer). Power was supplied to the upper electrode by a 13.56 MHz, 500W RF generator (Plasma Therm HFS 500 E). An automatic matching network minimized the reflected power to less than 1% of the forward power. Both forward and reflected power were monitored by a directional wattmeter (Bird 4410A). Light from the plasma emission was collected through a quartz side window through a pair of iris diaphragms to attain spatial resolution. The light was then focused onto one end of an optical fiber and was transmitted to the entrance slit of a monochromator (Jarrell-Ash Monospec 27) having a 1200 grooves/mm diffraction grating. The light passing through the exit slit was detected by a photomultiplier tube (Hamamatsu R955 HA) driven by a photometer (Pacific Instruments, 126D). A long pass filter (>495 nm) was used to avoid second-order interference in the light emission spectrum which was displayed on a strip chart recorder. The optical train was mounted on a translation stage (Newport M-416) and a 2 mW He-Ne laser (Hughes H-3022P) was used to align the optical components. With this system a cylinder of light along a horizontal plane (parallel to the electrodes) could be collected with a spatial resolution better than 1 mm. This resolution was thought to be adequate for measuring radial light emission intensity profiles.

Experimental system and data analysis.—The purpose of the experimental work was to study the active species concentration profiles and their dependence on plasma reactor operating conditions; and in turn to test the predictions of the mathematical model. The oxygen plasma was chosen as a model experimental system because the glow discharge reactions are better known as compared to other systems. In addition, the electron energy and electron density could be estimated as a function of power, pressure, and reactor geometry (20). Thus, there was no need to treat the former two quantities as adjustable parameters as is usually done in published plasma etching works. Further, a silver oxide (Ag_2O) film was used as the reactive substrate. The film was prepared by coating part of the lower electrode with a silver paint. When the coating was exposed to an oxygen plasma, the organic binder burned and the remaining silver turned into black silver oxide. Silver oxide is known to be catalytic towards surface recombination of atomic oxygen, the main etchant species in an oxygen plasma. The silver oxide/oxygen plasma system was thought to simulate etching of a thin film. Using a silver oxide film instead of an etchable material (*e.g.*, polymer in the case of oxygen plasma) had several advantages. First, the coupling of the plasma to ground was nearly uniform as compared to possible nonuniformities of plasma coupling through a silicon wafer resting on the electrode (16). Second, contamination of the plasma by reaction products was absent; the surface reaction on the silver oxide was simply the recombination of atomic oxygen to yield molecular oxygen. Thus, the discharge could be regarded as one in pure oxygen. Hence, data for the pure oxygen plasma could be used for calculations, and any reactant concentration gradients would be due to differences in reactivity between the Ag_2O film and the surrounding electrode surface. Furthermore, the Ag_2O film was not consumed and a large number of experiments could be performed on the same film without opening the reaction chamber to the atmosphere. This enhanced experimental reproducibility.

Optical emission spectroscopy (OES) with an actinometer gas (31) was employed to obtain the reactant (O atom) concentration profiles. In OES, the intensity of light emitted by a species may be related to the ground state concentration of that species. The pertinent reactions can be written as

$$O + e \xrightarrow{k_e} O^* \qquad [R6]$$

$$O^* \xrightarrow{k_S} O + h\nu \qquad [R7]$$

$$O^* + M \xrightarrow{k_q} O + M \qquad [R8]$$

Reaction [R6] is the excitation of species O by electron impact. The excited species O* can decay by spontaneous emission [R7] or by quenching upon collision with other species [R8]. If reaction [R8] can be neglected, the spontaneous emission intensity is proportional to the ground state concentration [O]

$$i_o \sim k_e n_e [O] \qquad [39]$$

The above analysis assumes electron-impact excitation as the dominant mechanism for producing O*. For example, a reaction of the type

$$O_2 + e \rightarrow O^* + O \qquad [R9]$$

would invalidate actinometry if the corresponding O* atom were to emit at the wavelength of interest. However, in Eq. [39], the so-called excitation efficiency $\eta_e = k_e n_e$ varies with the reactor operating conditions. In order to account for this variation, Coburn and Chen (31) introduced a small amount of an inert gas (actinometer) which has an excitation threshold and a cross section similar to the species of interest. This way, although the individual η_e values for the actinometer and the species of interest change with operating conditions, their ratio remains almost constant. Hence by writing an equation similar to Eq. [39] for the actinometer gas (say Ar), and taking their ratio results

$$\frac{i_o}{i_{Ar}} = q \frac{[O]}{[Ar]} \qquad [40]$$

where q is a proportionality constant and [Ar] is the known concentration of the actinometer. By measuring i_o and i_{Ar} at the appropriate wavelengths, the relative change in [O] can be obtained. In the present study, the 8446Å O atom line and the 7504Å Ar line were used (32). The stronger 7774Å O atom line was not used because it was shown not to obey the basic assumptions of actinometry {reaction [R9] was found to be important for this line, see Ref. (32)}. A 5% mol fraction of the actinometer gas was used. It was found that Ar additions of up to 6% did not affect the oxygen plasma emission.

Figure 3 shows a cross section of the radially symmetric glow taken at a certain plane parallel to the electrodes (say at $z = z_o$). The optical train collected light from a small plasma volume, as shown in the figure. By translating the optics parallel to the x-axis, light from different locations was collected and the intensity $I(x, z_o)$ measured. The latter can be related to the local emission intensity $i(r, z_o)$ by

$$I(x, z_o) = 2 \int_x^R \frac{r\Omega(x, r)}{\sqrt{r^2 - x^2}} i(r, z_o)\, dr \qquad [41]$$

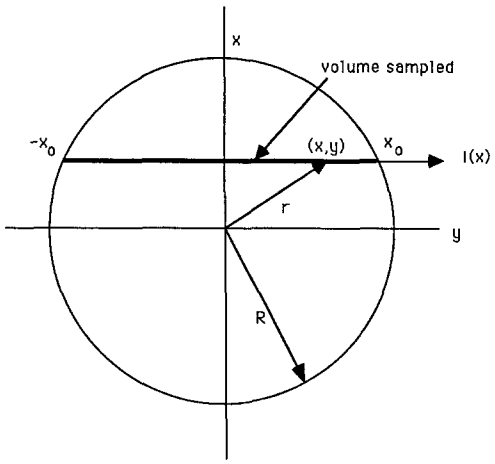

Fig. 3. Cross section of plasma glow showing small volume over which light emission $I(x)$ was collected.

where

$$\Omega(x, r) = \exp\{-\alpha(\sqrt{R^2 - x^2} - \sqrt{r^2 - x^2})\} + \exp\{-\alpha(\sqrt{R^2 - x^2} + \sqrt{r^2 - x^2})\} \quad [42]$$

Equation [41] accounts for radiation trapping with a constant absorption coefficient, α. For sufficiently small α, Eq. [41] reduces to

$$I(x, z_o) = 2\int_x^R \frac{ri(r, z_o)\,dr}{\sqrt{r^2 - x^2}} \quad [43]$$

The last integral was inverted by applying the Abel transform to yield (33)

$$i(r, z_o) = -\frac{1}{\pi}\int_r^R \frac{I'(x, z_o)\,dx}{\sqrt{x^2 - r^2}} \quad [44]$$

where $I'(x, z_o) = dI(x, z_o)/dx$. Equation [44] was numerically integrated using the measured values of $I(x, z_o)$ by Fries' technique (34). Thus the radial local intensity profile was obtained.

The resulting profile (especially close to $r = 0$) was found to be sensitive to the scatter of the $I(x, z_o)$ experimental data. The sensitivity was minimized by smoothing the data. At a given axial position $z = z_o$, radial emission intensity profiles $i(r, z_o)$ were obtained for both O atoms and Ar. Equation [45] (similar to Eq. [40]) was then applied to find the ground state O atom concentration profile

$$C_o(r, z_o) = \frac{1}{q} C_{Ar} \frac{i_o(r, z_o)}{i_{Ar}(r, z_o)} \quad [45]$$

Note that since Ar is not reactive, C_{Ar} is independent of position. The above procedure was repeated at a different axial position. Hence a three-dimensional mapping of the reactant concentration profile was realized.

Results and Discussion

The three-dimensional velocity profiles are plotted in Fig. 4 for a wall Reynolds number $R_w = 1.0$. Figure 4a is a plot of the dimensionless radial velocity profile ($2U/AW_w = \xi f'(\zeta)$, see Eq. [7]). The radial velocity is zero at the reactor

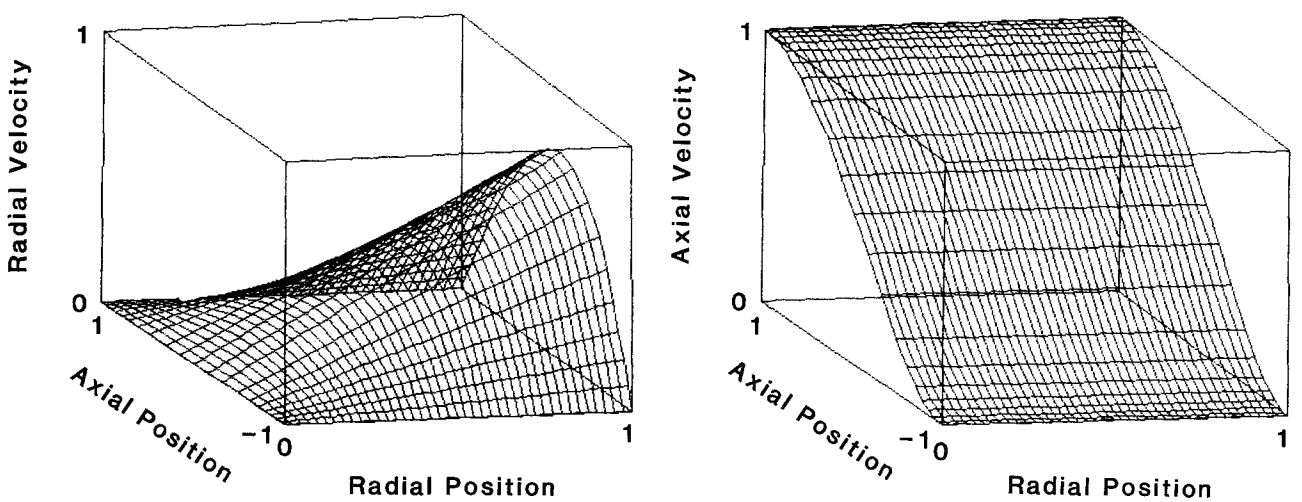

Fig. 4. (a, left) Dimensionless radial gas velocity profile for a wall Reynolds number $R_w = 1$. (b, right) Dimensionless axial gas velocity profile for a wall Reynolds number $R_w = 1$.

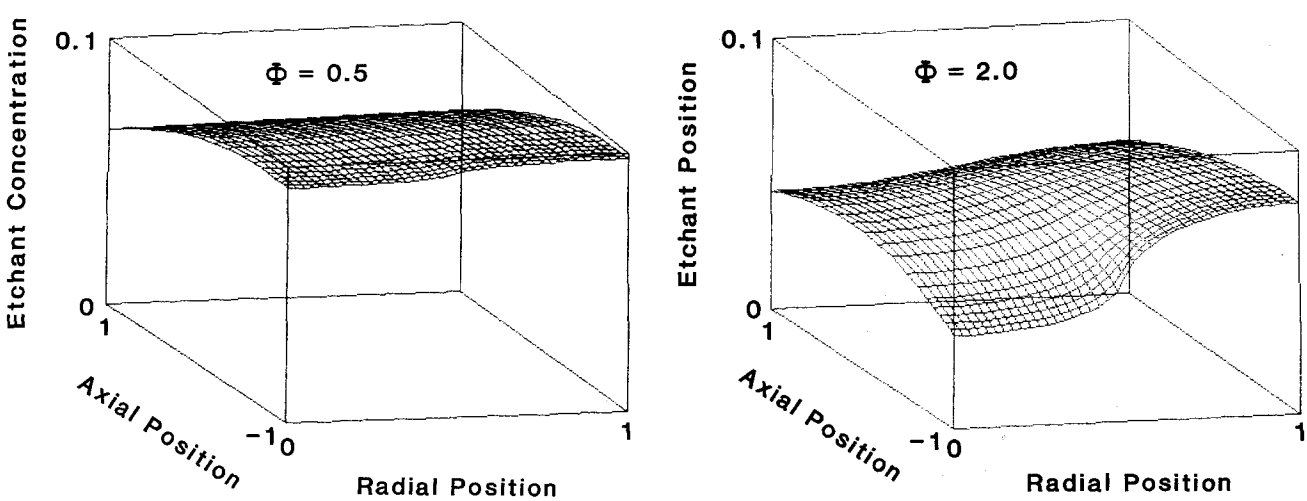

Fig. 5. (a, left) Dimensionless etchant concentration distribution for Thiele modulus $\Phi_n = 0.5$. Other conditions were $Pe = \theta_e = 1$, $Da = 0.5$, $A = 5$, $\Phi_+ = \beta_1 = \gamma_a = \gamma_c = \delta = Co = 0$. The wafer radius was half of the lower electrode radius. (b, right) The same as in Fig. 5a but with $\Phi_n = 2$.

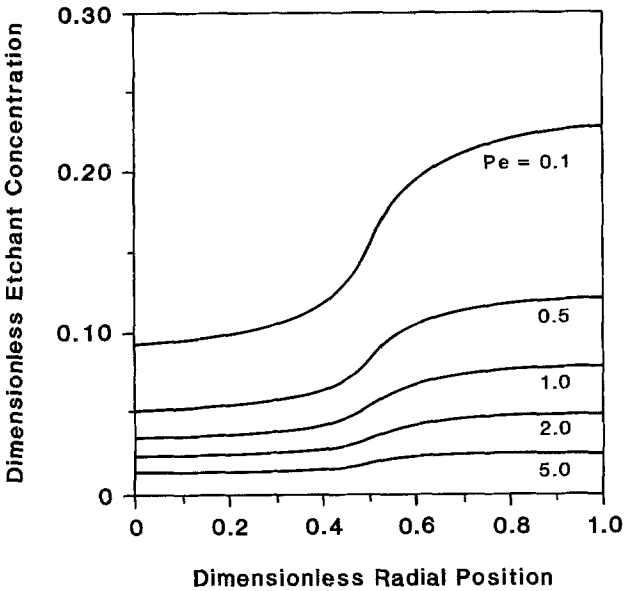

Fig. 6. Dimensionless etchant concentration distribution as a function of the dimensionless radial position along the substrate electrode surface, for different values of the Peclet number, Pe. Conditions were otherwise as in Fig. 5b.

center and increases linearly towards the exit. At a given radial position, the radial velocity profile is close to being parabolic (Eq. [12] and [14]) for small values of R_w. Figure 4b is a plot of the dimensionless axial velocity profile ($|W/W_w|$, see Eq. [8]). The axial velocity is maximum at the upper electrode position through which gas enters and decreases monotonically with axial position to become zero at the lower electrode surface. The axial velocity profile is independent of radial position.

Figure 5 gives three-dimensional plots of the reactant concentration for two different values of the Thiele modulus Φ_n. Other parameters were assigned values as shown in the figure caption. For illustrative purposes, surface recombination, volume recombination, and ion-assisted reactions were neglected, and a uniform electron density profile was used. Since ion-assisted reactions were neglected, the following results pertain to situations for which chemical etching dominates. For small values of Φ_n, nearly uniform radial concentration profiles result (Fig. 5a). As Φ_n increases however (for example by increasing the wafer surface reactivity), the situation changes dramatically. Owing to rapid consumption of active species right on the wafer surface (in Fig. 5, as well as in Fig. 6 and 7, the wafer radius is half the electrode radius), a pronounced decrease in the etchant concentration occurs over the reactive surface (Fig. 5b). Under these conditions, diffusion is not rapid enough to supply reactant from the plasma volume above the relatively inert surrounding electrode. Hence large radial concentration gradients develop especially at the boundary between the wafer and the surrounding electrode (radial position $\xi_1 = 0.5$). If the etch rate increases monotonically with reactant concentration, such concentration gradients would result in the "bullseye" wafer clearing pattern. One further notes an axial concentration gradient above the reactive surface in Fig. 5b. Both radial and axial concentration gradients become milder as one moves further away from the wafer surface. In addition, owing to the limited supply of active species by dissociation in the plasma, an increase in wafer reactivity (larger k_n and hence larger Φ_n) results in lower reactant concentration as seen by comparing Fig. 5a and b. However this does not necessarily imply a lower etch rate since the etch rate depends on the reaction rate constant as well. In fact, although the etch uniformity degrades, the etch rate increases with Φ_n. The reactant concentration is lower at the upper electrode (plane at axial position $\zeta = 1$ in Fig. 5a) due to convective removal of reactant away from the electrode by the entering gas.

The effect of the Peclet number, Pe, on the etchant radial concentration profiles right above the substrate electrode surface ($\zeta = -1$) is shown in Fig. 6. As Pe increases (*e.g.*, by increasing flow rate), the concentration gradients are alleviated resulting in improved etch uniformity. However, the etch rate decreases with increasing Pe because of convective removal of active species out of the reactor. The etch rate decreases drastically with Pe at low values of Pe, but the etch rate is not as sensitive at high values of Pe. In summary, the etch rate improves as Φ_n increases and Pe decreases, but the etch uniformity improves with a lower Φ_n and a higher Pe. Clearly there are optimum parameter settings for which the etch rate is maximized given an acceptable degree of nonuniformity.

Etching uniformity improves if the electrode surrounding the wafer is reactive towards the etchant species (*e.g.*, by surface recombination reaction). This is shown in Fig. 7 where the uniformity index, *UI*, is plotted against the reaction selectivity, *S*. The uniformity index is defined as

$$UI = \frac{R_{max} - R_{min}}{2R_{av}} \qquad [46]$$

where R_{max}, R_{min}, R_{av} are the maximum, minimum, and average etch rate, respectively, along the wafer radius. The uniformity improves as *UI* decreases. The reaction selectivity is defined as

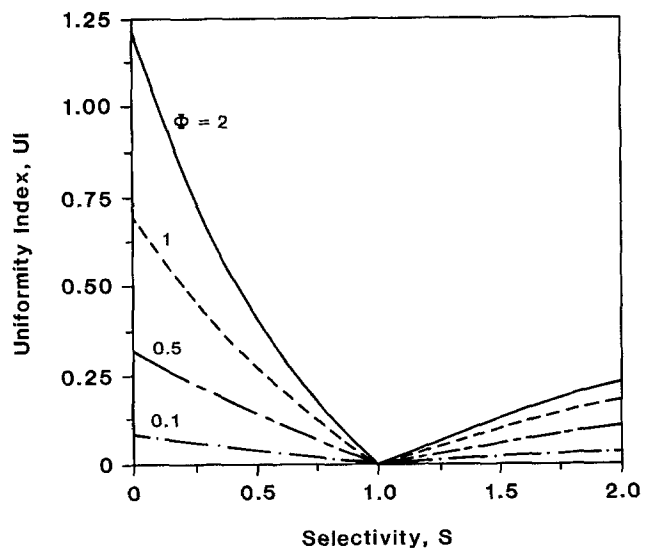

Fig. 7. Uniformity index as a function of reactor selectivity for different values of the Thiele modulus Φ_n. Other conditions were the same as in Fig. 5b except that γ_o was varied such that $\gamma_o/\Phi_n = k_o/k_n = S$ (selectivity).

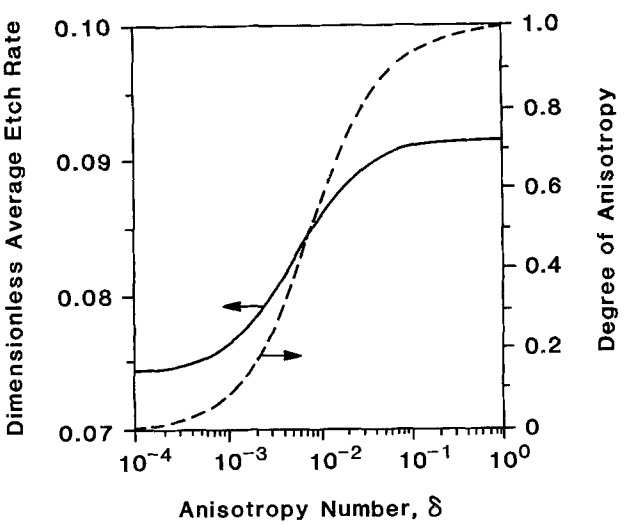

Fig. 8. Dimensionless average etch rate and degree of anisotropy as a function of the anisotropy number δ. Other conditions were $\Phi_n = 2$, $\Phi_+ = \sqrt{8}$; Pe = $\theta_e = 1$; Da = Co = 0.5; $A = 5$; $\beta_1 = \gamma_o = \gamma_c = 0$; $V_s^* = -50$.

$$S = \frac{\text{Reaction rate on the surface surrounding the wafer}}{\text{Reaction rate on the wafer surface}} \quad [47]$$

Zero selectivity implies an inert surrounding electrode surface, and gives the worst uniformity. Regardless of the degree of reactivity of the wafer (value of Φ_n), etching is uniform if the surrounding electrode surface has a similar reactivity ($S = 1$). This result is in contrast to the Reinberg-type radial flow reactor, where radial nonuniformities can be present even if the whole substrate electrode area has the same reactivity (7). When $S < 1$, a "bullseye" film clearing pattern results. When $S > 1$, the inverse film clearing pattern results (*i.e.*, the etch rate decreases monotonically from the wafer center to the wafer periphery). A method of improving etch uniformity is to cover the electrode area surrounding the wafer with a material having a reactivity similar to that of the wafer. Such action however may result in a decreased etch rate owing to loading.

However, etch rate and uniformity are not the only important variables in plasma etching. One also desires to achieve a high degree of anisotropy. Figure 8 shows the effect of the anisotropy number δ on the average etch rate (defined by the right-hand side of Eq. [31]) and the degree of anisotropy, An, defined by Eq. [38]. A value of An close to zero implies isotropic etching whereas a value of An close to unity implies vertical (anisotropic) etching. For low values of δ (*e.g.*, low ion flux and energy) chemical etching dominates (*i.e.*, reaction [R5] is negligible) and isotropic etching results. The degree of anisotropy improves with increasing δ and, at high δ, where ion-assisted etching dominates, the degree of anisotropy approaches unity. The etch rate too approaches an asymptotic value at high δ, because the process is then limited by the reactant supply to the surface.

Comparison of model with experimental data.—The model predictions were compared with experimental data of reactant concentration profiles obtained by spatially resolved optical emission spectroscopy as outlined in the Experimental section. Transport and reaction parameters of the pure oxygen discharge were used as before (20). The experimental conditions are summarized in Table I. In order to achieve plasma confinement, low power and high pressure conditions were used. The substrate was a Ag_2O film partly covering the lower electrode. Reaction on the substrate and gas flow were found to be the dominant reactant (O atom) loss mechanisms. Therefore surface recombination was neglected. The substrate reaction was assumed to be of first order and the corresponding rate constant was fit to $k_n = 40.8$ cm/s. A flat electron density profile was assumed. The data below was taken midway between the electrodes unless otherwise noted.

Table I. Parameter values for system studied

Parameter	Value
Pressure	1-3 torr
Power	20-50W
Gas flow rate	25-100 sccm
Diameter of reactive film	7.5-10 cm
Frequency	13.56 MHz

Figure 9 shows the atomic oxygen mole fraction as a function of radial position for three different values of power into the plasma. Figure 9a is the case of an empty reactor, *i.e.*, no Ag_2O film on the electrode surface. The concentration is nearly uniform close to the reactor center and decreases monotonically further away. The concentration is higher at higher power due to increased etchant production. A dramatic change in the concentration profile occurs (Fig. 9b), when part of the lower electrode is coated with Ag_2O in the form of a concentric disk having a diameter of 75 mm (loaded reactor). A "dip" in the O atom concentration profile occurs over the reactive surface and large concentration gradients appear, especially around the boundary between active and relatively inert surfaces (*i.e.*, around the 3.75 cm position). As the power increases, the reactant concentration gradients become steeper. This is because at high power the reactant is produced faster than it can diffuse (*i.e.*, larger value of the Damköhler number Da, see Eq. [34]). Further, the reactant concentration is substantially lower in the case of a loaded reactor because of increased reactant losses. The model predictions are shown with the solid lines. The model does not predict the drop in concentration close to the reactor exit, in the empty reactor case. A better agreement could have been obtained in this case if the electron density profile were assumed to be of the form of Eq. [17], instead of a uniform electron density.

The effect of pressure is shown in Fig. 10. At lower pressures the diffusivity increases ($D \sim P^{-1}$) and concentration gradients are smaller (*i.e.*, smaller Φ_n). However, the reactant concentration decreases with decreasing pressure. The model predictions (solid lines) agree relatively well with the data. The effect of flow rate is shown in Fig. 11. In accordance with the previous discussion (Fig. 6) a higher flow rate results in better uniformity, but at the same time

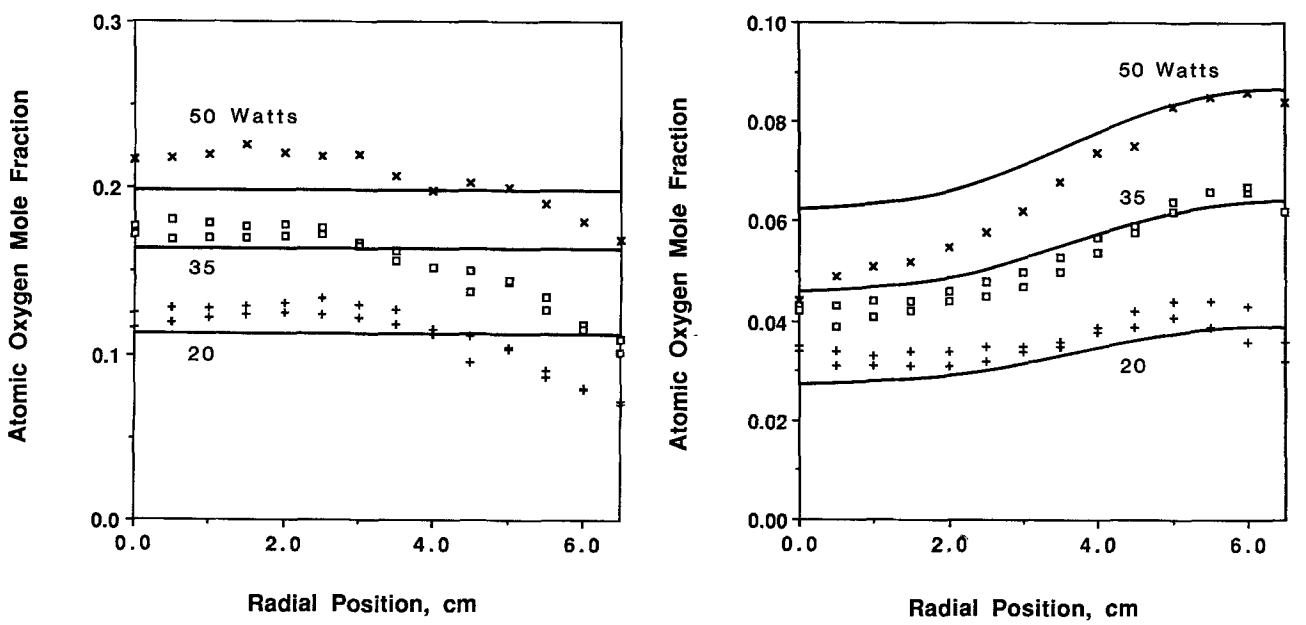

Fig. 9 (a, left) Atomic oxygen mole fraction vs. radial position in an empty reactor. Other conditions were $P = 2$ torr and $Q = 100$ sccm. Experimental data: x ~ 50, □ ~ 35, + ~20W. Solid lines are model predictions. (b, right), As in Fig. 9a but in a loaded reactor. Reactive film radius was 3.75 cm. Solid lines are model predictions.

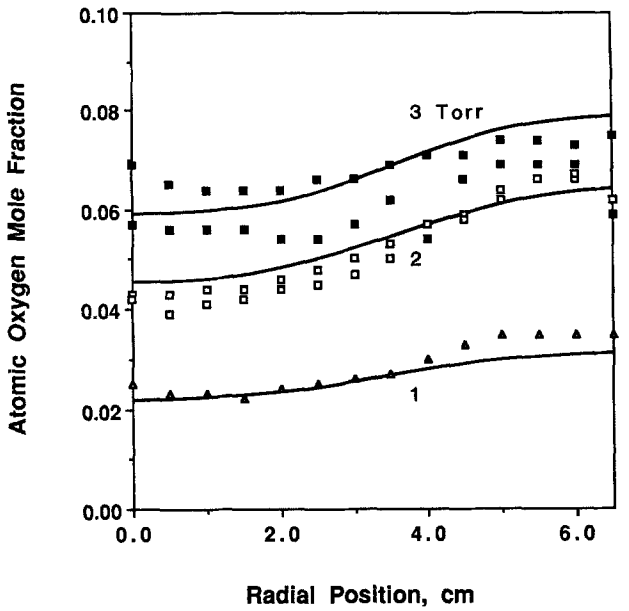

Fig. 10. Atomic oxygen mole fraction vs. radial position in a loaded reactor with a reactive film radius of 3.75 cm. Other conditions were Po = 35W and Q = 100 sccm. Experimental data: ■ ~ 3, □ ~ 2, Δ ~ 1 torr. Solid lines are model predictions.

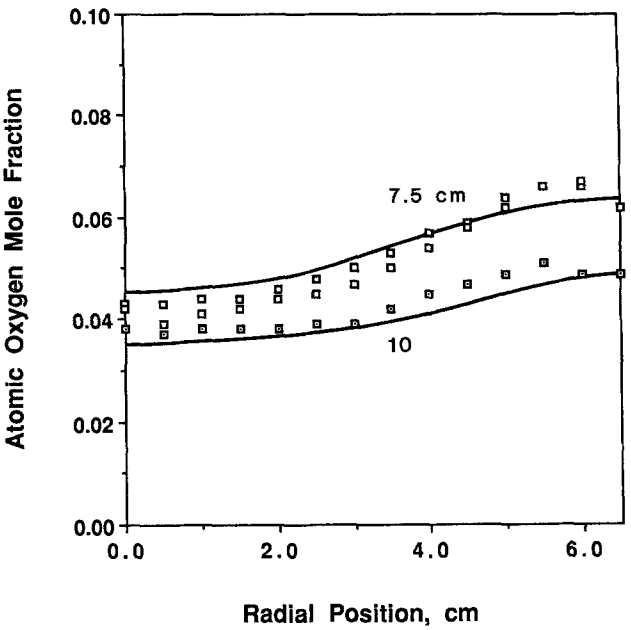

Fig. 12. Atomic oxygen mole fraction vs. radial position in a loaded reactor with two different reactive film radii. Other conditions were Po = 35W, Q = 100 sccm, and P = 2 torr. Experimental data: □ ~ reactive film radius 3.75 cm, ⊡ ~ reactive film radius 5 cm. Solid lines are model predictions.

the etch rate decreases. The effect of surrounding the active surface by one with a similar reactivity is seen in Fig. 12, where the concentration profiles resulting from two different Ag_2O film diameters are compared. The 10 cm diam film can be thought of as a 7.5 cm diameter film surrounded by a 1.25 cm wide ring of equal reactivity. The concentration profile is more uniform for the larger diameter film, at the expense of a lower reactant concentration due to increased loading.

Axial O atom concentration profiles were also obtained. Concentration gradients were very weak in the empty reactor case (Fig. 13a), implying negligible surface reaction. However, significant concentration gradients were observed in the loaded reactor (Fig. 13b), implying a fast surface reaction. Optical emission data close to and within the sheath (the sheath was visually observed to be a few mm thick under typical conditions) should be viewed with caution because processes other than direct electron impact may be responsible for excitation (*e.g.*, collisions with ions or fast neutrals). More reliable data in the sheath can be obtained by laser induced fluorescence (LIF). Nevertheless, OES data from outside the sheath may be extrapolated to obtain the surface concentration and flux. In summary, considering the wide range of experimental conditions studied, the model predictions were in good quantitative agreement with the experimental data.

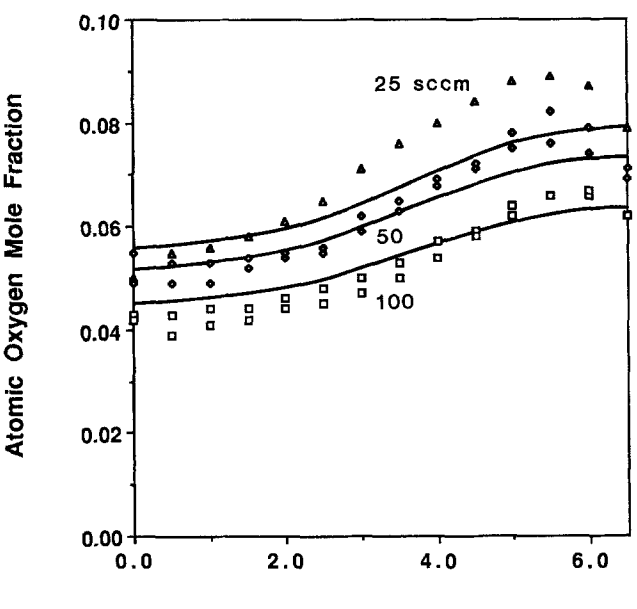

Fig. 11. Atomic oxygen mole fraction vs. radial position in a loaded reactor with a reactive film radius of 3.75 cm. Other conditions were Po = 35W and P = 2 torr. Experimental data: Δ ~ 25, ◇ ~ 50, □ ~ 100 sccm. Solid lines are model predictions.

Summary and Conclusions

A two-dimensional transport and reaction model of a single-wafer parallel plate plasma reactor was presented. Emphasis was placed on high pressure (~1 torr), high frequency (13.56 MHz) operating conditions. Given the surface reaction kinetics, the model was capable of predicting both etch uniformity and anisotropy. The uniformity of chemical etching was studied as a function of important system parameters. It was found that the ratio of the reactivity of the surrounding electrode surface as compared to that of the wafer surface, S, critically affected uniformity. Regardless of the degree of wafer reactivity, the uniformity was improved as S approached unity. A bullseye clearing pattern was predicted for $S < 1$ and the reverse pattern for $S > 1$. In the case of $S \neq 1$, the uniformity became worse the larger the departure of S from unity. In such case, the absolute uniformity was improved by surrounding the wafer with a material of similar reactivity, by increasing the flow rate, or by decreasing the reactor pressure or power. However such actions also served to decrease the etch rate. Further, for a given substrate electrode material, increasing the wafer reactivity resulted in a higher etch rate (despite the lower etchant species concentration) but a poorer etch uniformity. Under otherwise identical conditions, the etch rate was found to be insensitive to the flow rate at high flow rates.

The oxygen plasma was used as a model experimental system to test the theoretical predictions. One advantage was that the electron density and temperature could be estimated as a function of pressure and power, and there was no need to treat the former two quantities as adjustable parameters, as done in other published works. A silver oxide film coating part of the substrate electrode was used to simulate etching of a thin film. The advantages were (*i*) no contamination of the plasma with etching by-products and (*ii*) uniform plasma coupling to ground through the substrate grounded electrode. An experimental technique

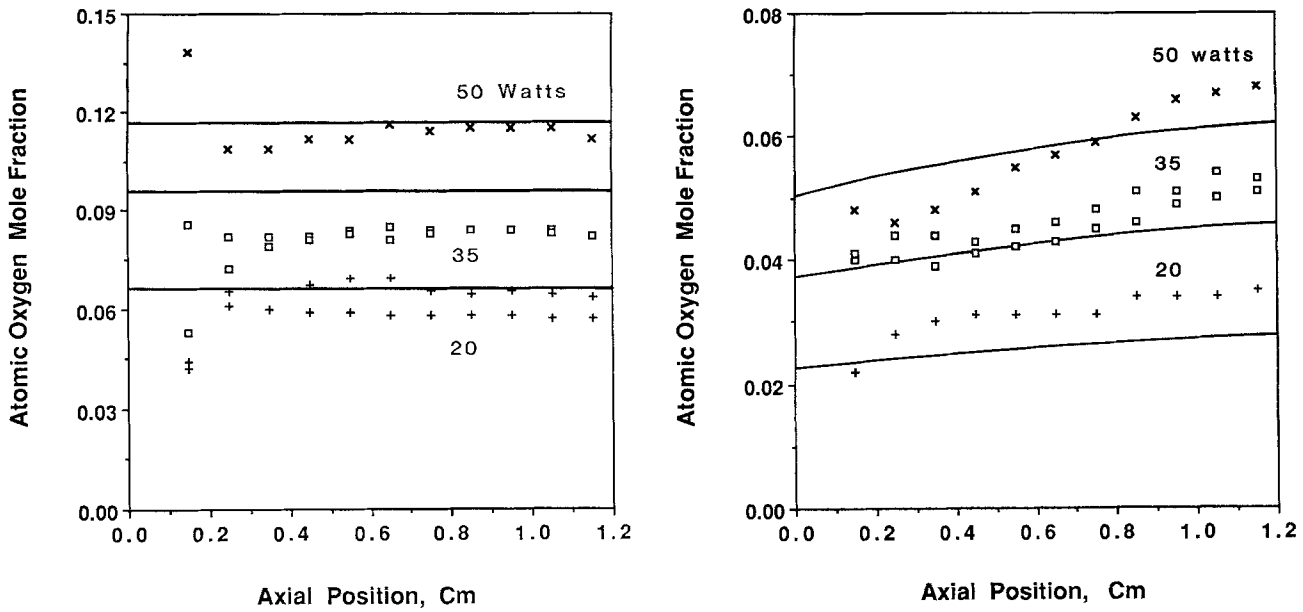

Fig. 13. (a, left) Atomic oxygen mole fraction vs. axial position in an empty reactor. Conditions were Po = 35W, Q = 100 sccm, and P = 2 torr. Experimental data: x ~ 50, □ ~ 35, + ~ 20W. Solid lines are model predictions. (b, right) Atomic oxygen mole fraction vs. axial position in a loaded reactor with a reactive film radius of 3.75 cm. Other conditions were as in Fig. 13a. Solid lines are model predictions.

based on spatially resolved optical emission spectroscopy in concert with actinometry and the Abel transform was developed to obtain a three-dimensional mapping of the active species (O atoms) concentration profile. In the absence of a reactive film (empty reactor), the etchant concentration was uniform close to the reactor center and decreased monotonically towards the reactor exit. With a reactive film present (loaded reactor), a dramatic change in the etchant concentration profile occurred. A profound decrease in concentration occurred over the reactive surface and large concentration gradients appeared at the boundary of the reactive film with the surrounding electrode. Axial concentration profile measurements revealed concentration gradients close to the reactive surface. Good quantitative agreement was observed between the model predictions and the experimental data over the range of pressure, power, flow rate, and reactive film radius studied.

The experimental system was chosen carefully such that conditions were as well defined as possible. For example, the silver oxide film coating the substrate electrode was in intimate contact with the cooled electrode. Hence a constant film temperature could be assumed. However, in practical systems, etching films are on silicon wafers which often simply rest on the substrate electrode. The wafer temperature may then be very different from the electrode temperature. Moreover, if a temperature distribution exists on the wafer surface, etch rate and uniformity will be affected. Such effects can be added in further refinements of the model.

The present model does not apply in the low pressure (<0.25 torr), low frequency (<3 MHz) regime, and knowledge of the reaction kinetics is needed to apply the model to different reactive plasma systems. Despite its limited applicability, the present model can serve as a basis for further additions and refinements. The good quantitative agreement with experimental data demonstrated that relatively simple engineering models can be useful tools in the design and scale-up of plasma etching and deposition systems. In addition, the experimental technique developed to monitor the three-dimensional etchant concentration profiles is much cheaper and easier to implement than competing techniques such as LIF, should be readily adaptable to existing or new plasma etching systems, and may serve as an *in situ* etch uniformity monitor.

Acknowledgments

This work was financially supported in part by the National Science Foundation (CBT-8708908) and by Texas Instruments, Incorporated. We are grateful to Dr. Gabe Barna of Texas Instruments for technical support.

Manuscript submitted March 18, 1988; revised manuscript received July 22, 1988.

The University of Houston assisted in meeting the publication costs of this article.

LIST OF SYMBOLS

An	degree of anisotropy, Eq. [24]
A	aspect ratio (r_2/L)
C	species concentration, mol/cm^3
Co	collision number, Eq. [37]
D	diffusion coefficient, cm^2/s
Da	Damköhler number, Eq. [34]
I_+	ion current, (cm^2-s)$^{-1}$
I	light emission intensity, arbitrary units
i	local light emission intensity, arbitrary units
K_1	volume recombination rate constant, cm^6/mol^2-s
k	Boltzmann constant, 1.38066 10^{-23} J/K
k_{sub}	reaction rate constant, units vary (sub refers to appropriate subscript)
k_n	chemical (neutral) etching rate constant, cm/s
k_+	ion-assisted etching rate constant, cm/s
k_d	damage site formation rate constant, mol/eV
k_p	etchant production rate constant, cm^3/s
k_c, k_a	surface recombination rate constants, cm/s
L	half interelectrode gap, cm
M	molecular mass, g
m	electronic mass, g
N	neutral particle number density, cm^{-3}
n_e	electron number density, cm^{-3}
$\bar{n}_e$	average electron number density, cm^{-3}
P	pressure, dyne/cm^2 or torr
Pe	Peclet number, Eq. [33]
Q	gas flow rate, cm^3/s
q	proportionality constant, Eq. [40]
R_{sub}	reaction rate, units vary (sub refers to appropriate subscript)
R_g	gas constant, 62,358 torr-cm^3/mol-K
R_w	wall Reynolds number
r	radial coordinate, cm
r_1	wafer radius, cm
r_2	reactor radius, cm
T_g	gas temperature, K
T_e	electron temperature, K
u_R	reference ion velocity, Eq. [36], cm/s
U	radial gas velocity, cm/s
UI	uniformity index, Eq. [46]
v_1	thermal velocity of atoms, cm/s
V_s	sheath voltage, V
W	axial gas velocity, cm/s
W_w	wall velocity, cm/s
w	wall recombination coefficient
x, y	Cartesian coordinates, cm
z	axial coordinate, cm

Greek

α	absorption coefficient, cm^{-1}, Eq. [42]
β_1	dimensionless grouping, Eq. [34]
γ	dimensionless grouping, Eq. [35]
δ	dimensionless grouping, Eq. [36]
ϵ	energy, eV
ζ	dimensionless axial coordinate
η	excitation efficiency
θ_i	dimensionless atomic species concentration
θ_e	dimensionless electron number density, Eq. [32]
λ_D	Debye length, cm
ν	gas kinematic viscosity, cm^2/s
ξ	dimensionless radial coordinate
ρ	gas density, g/cm^3
σ	collision cross section, cm^2
Φ	Thiele modulus, Eq. [35]

Subscripts

a	anode
c	cathode
d	"damaged" site
e	electrons
g	gas
n	neutral (chemical)
t	total
v	volume
+	positive ions or ion-assisted
1	atomic
2	molecular

Superscript

*	dimensionless quantity or excited species

REFERENCES

1. "VLSI Electronics: Microstructure Science," Vol. 8, "Plasma Processing for VLSI," N. G. Einspruch and D. M. Brown, Editors, Academic Press, Inc., New York (1984).
2. M. J. Kushner, *J. Appl. Phys.*, **53,** 2923 (1982); *ibid.*, **53,** 2939 (1982).
3. I. C. Plumb and K. R. Ryan, *Plasma Chem. Plasma Process.*, **6,** 205 (1986); *ibid.*, **6,** 231 (1986).
4. D. B. Graves and K. F. Jensen, *IEEE Trans. Plasma Sci.*, **PS-14** (2), 78 (1986); see also other papers in April 1986 issue of that journal.
5. M. S. Barnes, T. J. Colter, and M. E. Elta, *J. Appl. Phys.*, **61,** 81 (1987).
6. G. Rogoff, J. Kramer, and R. Piejak, *IEEE Trans. Plasma Sci.*, **PS-14** (2), 103 (1986).
7. M. Dalvie, K. F. Jensen, and D. B. Graves, *Chem. Eng. Sci.*, **14,** 653 (1986).
8. E. Zawaideh and N. S. Kim, *J. Appl. Phys.*, **62,** 2498 (1987).
9. D. Edelson and D. Flamm, *ibid.*, **56,** 1522 (1984).
10. L. E. Kline, *IEEE Trans. Plasma Sci.*, **PS-14** (2), 145 (1986).
11. R. Gottscho and T. Miller, *Pure Appl. Chem.*, **56,** 189 (1984).
12. V. M. Donnelly, D. L. Flamm, and R. H. Bruce, *J. Appl. Phys.*, **58,** 2135 (1985).
13. B. Lipschultz, I. Hutchinson, B. LaBombard, and A. Wan, *J. Vac. Sci. Technol.*, **A4,** 1810 (1986).
14. R. C. Alkire and D. J. Economou, *This Journal*, **132,** 648 (1985).
15. J. W. Coburn, *J. Vac. Sci. Technol.*, **A4,** 1830 (1986).
16. A. G. Nagy, *This Journal*, **131,** 1871 (1984).
17. G. S. Selwyn, *J. Appl. Phys.*, **60,** 2771 (1986).
18. G. K. Herb, D. J. Rieger, and K. Shields, *Solid State Technol.*, 109 (Oct. 1987).
19. D. A. Danner and D. W. Hess, *This Journal*, **133,** 151 (1986).
20. D. J. Economou and R. C. Alkire, *ibid.*, **135,** 2786 (1988).
21. R. A. Gottscho, G. P. Davis, and R. H. Burton, *J. Vac. Sci. Technol.*, **A1,** 622 (1983); *Plasma Chem. Plasma Process.*, **3,** 193 (1983).
22. H. Schlichting, "Boundary Layer Theory," 7th ed., McGraw-Hill, Inc., New York (1979).
23. A. H. Nayfed, "Perturbation Methods," John Wiley & Sons, Inc., New York (1972).
24. D. J. Economou, D. R. Evans, and R. C. Alkire, *This Journal*, **135,** 756 (1988).
25. D. L. Flamm, *J. Vac. Sci. Technol.*, **A4,** 729 (1986).
26. A. T. Bell, in "Techniques and Applications of Plasma Chemistry," J. R. Hollahan and A. T. Bell, Editors, John Wiley & Sons, Inc., New York (1974).
27. J. C. Graves and J. W. Linnett, *Trans. Faraday Soc.*, **55,** 1355 (1959).
28. D. L. Flamm and V. M. Donnelly, *Plasma Chem. Plasma Process.*, **1,** 317 (1981).
29. J. W. Coburn, *ibid.*, **2,** 1 (1982).
30. V. M. Donnelly, D. L. Flamm, W. C. Dautremont-Smith, and D. J. Werder, *J. Appl. Phys.*, **55,** 242 (1984).
31. J. W. Coburn and M. Chen, *ibid.*, **51,** 3134 (1980).
32. R. E. Walkup, K. L. Saenger, and G. S. Selwyn, *J. Chem. Phys.*, **84,** 2668 (1986).
33. C. J. Cremers and R. C. Birkebak, *Appl. Opt.*, **5,** 1075 (1966).
34. W. Frie, *Ann. Phys.*, **10,** 332 (1963).